https://doi.org/10.5194/egusphere-2026-302
Preprint. Discussion started: 11 February 2026

Impacts of entrainment on secondary ice production in deep convective clouds

Bowen Z. Portman[1], Paul J. Connolly[1], Alan M. Blyth[2], Rachel L. James[1], and Huihui Wu[1*]

[1]Department of Earth and Environmental Sciences, The University of Manchester, Manchester, UK
[2]National Centre for Atmospheric Science, University of Leeds, Leeds, UK
[*]Now at: Univ Paris Est Créteil and Université Paris Cité, CNRS, LISA, 94010 Créteil, France

Correspondence: Paul J. Connolly (paul.connolly@manchester.ac.uk)

Abstract.

The accurate representation of Secondary Ice Production (SIP) is essential for describing the microphysics of deep convective clouds, yet the exact mechanisms and efficiencies of SIP are still uncertain. In this study, we used the University of Manchester bin microphysics parcel model to investigate four SIP parameterisations: rime splintering, ice–ice collisional breakup, spherical freezing fragmentation of drops (mode 1), and fragmentation between supercooled droplets and more massive ice particles (mode 2). We simulated air trajectories through deep convective clouds observed during the Deep Convective Microphysics EXperiment (DCMEX) field campaign. Our results show that mode 2, as currently understood and represented in the model, is the key mechanism for explaining the high ice particle concentrations observed. We also present the first systematic study of how different entrainment conditions (adiabatic, homogeneous, and inhomogeneous) affect SIP mechanisms. In our simulations, homogeneous and inhomogeneous mixing with aerosol entrainment provide reasonable agreement with cloud-core and cloud-edge microphysical properties observed during DCMEX, respectively. The entrainment of external aerosols was also found to accelerate the collision–coalescence process under homogeneous mixing, leading to earlier ice enhancement. Our results show that SIP mechanisms, which are dependent on large droplets, such as mode 2, are highly sensitive to different entrainment conditions, emphasising the importance of representing entrainment correctly when including SIP processes in large-scale models.

1 Introduction

Ice formation in clouds significantly influences cloud properties and precipitation processes, thereby impacting weather systems and global climate (Planche et al., 2014; Field and Heymsfield, 2015; Tan et al., 2025). However, the formation pathways of ice crystals in clouds remain uncertain, as observed concentrations of ice particles often far exceed what can be explained by primary ice nucleation alone (Hallett et al., 1978; Blyth and Latham, 1993; Crawford et al., 2012; Lasher-Trapp et al., 2021; Lloyd et al., 2024). Several secondary ice production (SIP) mechanisms have therefore been proposed to explain this discrepancy (Phillips et al., 2018; Korolev et al., 2020). In our study, we focus on four SIP processes: rime splintering, ice–ice collisions, spherical freezing fragmentation of drops (mode 1), and fragmentation between supercooled droplets and more massive ice particles (mode 2).

https://doi.org/10.5194/egusphere-2026-302
Preprint. Discussion started: 11 February 2026

Rime-Splintering (RS), also known as the Hallett–Mossop process, is currently the most widely implemented SIP mechanism in cloud microphysics models, which occurs only within a narrow temperature range of -3 to -8 °C (Hallett and Mossop, 1974a) and requires the coexistence of droplets smaller than 12 μm and larger than 24 μm in diameter (Mossop, 1978; Harris-Hobbs and Cooper, 1987). However, the large amounts of ice observed in deep convective clouds cannot always be explained by RS, especially in cases where the increase in ice number is too rapid, the temperatures and crystal habits fall outside the RS window, or the necessary conditions for RS are not satisfied (Rangno and Hobbs, 1991; Lawson et al., 2015; Field et al., 2017). Recent experiments Seidel et al. (2024) also failed to reproduce the high SIP rates reported in earlier RS studies, thereby questioning the significance of rime splintering under mixed-phase convective conditions. As noted in the review by Korolev et al. (2020), the physical mechanism of RS remains poorly quantified and understood, with the parameterisation still highly uncertain. Therefore, SIP mechanisms that are less constrained by temperature and droplet spectrum conditions, such as Ice–ice collisional breakup and droplet shattering, may be able to explain the observed ice enhancement. However, parametrisations of these other SIP processes are perhaps just as uncertain as for the RS process.

Ice-Ice Collisional Breakup (CB) is the second SIP mechanism investigated in this study. This process refers to the mechanical fragmentation of ice particles during collisions, leading to the formation of new ice crystals. This mechanism has been observed in both aircraft measurements (Schwarzenboeck et al., 2009) and laboratory experiments (Vardiman, 1978; Takahashi and Nagao, 1995; Grzegorczyk et al., 2023). Laboratory studies found that CB is most active near $-16\,^{\circ}\mathrm{C}$ (Takahashi and Nagao, 1995), and field observations also showed substantial secondary ice near $-15\,^{\circ}\mathrm{C}$ (Mignani et al., 2019; Billault-Roux et al., 2023). In simulations of deep convective clouds during the HAIC/HIWC campaign, Grzegorczyk et al. (2025) found that ice–ice collisional breakup was a key contributor to ice enhancement, and that only when combined with rime-splintering could the observed high ice crystal concentrations be reproduced. However, the collision efficiency and fragmentation probability of this mechanism remain poorly understood, and future parameterisations will need to be improved accordingly (see the discussion in Korolev et al. 2020).

Finally, we examine the Drop-Freezing-Shattering (DS) mechanism, and we refer to the spherical freezing fragmentation of drops as mode 1 (M1) according to the description of Phillips et al. (2018). This mechanism has been identified in both field observations (Lawson et al., 2015) and laboratory experiments (Leisner et al., 2014; Lauber et al., 2018; Keinert et al., 2020). Many studies have incorporated M1 as a droplet fragmentation process in model simulations (Sotiropoulou et al., 2020; Huang et al., 2017; Grzegorczyk et al., 2025). However, James et al. (2023) found that its contribution was relatively minor in their simulations of an idealised shallow convective cloud.

We refer to the fragmentation between supercooled droplets and more massive ice particles as mode 2 (M2). To date, only one laboratory study has directly examined M2 (James et al., 2021), and its parameterisation still requires substantial testing. Nevertheless, many studies have already incorporated M2 into their investigations of SIP (Phillips et al., 2018; Sotiropoulou et al., 2020; Zhao and Liu, 2022; James et al., 2023), and James et al. (2023) suggested that M2 might be a key SIP mechanism in convective clouds where large droplets are present.

In this study, we aim to use the University of Manchester bin-microphysics parcel model (BMM, based on an updated version of the framework developed by James et al. 2023 and Fowler et al. 2020) to investigate secondary ice production in

https://doi.org/10.5194/egusphere-2026-302
Preprint. Discussion started: 11 February 2026

the deep convective clouds observed during the DCMEX campaign over New Mexico (Finney et al., 2024), and to explore the potential influence of different entrainment representations on SIP. The DCMEX field campaign was conducted in the Magdalena Mountains, where conditions are highly favourable for the development of multiple-thermal cumulus congestus convection limited to the mountain range that transitions to deeper thunderstorms (Finney et al., 2024). The occurrence of the clouds is strongly influenced by the North American Monsoon (NAM), when moist inflows from the Gulf of Mexico and the eastern Pacific occur between June and September (Adams and Comrie, 1997; Erfani and Mitchell, 2014). Wu et al. (2025) conducted a combined modelling and observational analysis of warm cloud processes in two DCMEX cases and also found that aerosol entrainment plays a key role in broadening the droplet size distribution (DSD), which is expected to be crucial for subsequent investigations of the ice phase in clouds. Previous work at the same site by Blyth and Latham (1993) suggested that RS was likely responsible for the high ice crystal concentrations observed in these clouds.

In previous modelling studies of deep convective clouds, conflicting conclusions have been reached regarding the dominant SIP mechanisms. While some studies suggest that DS provides the primary contribution (Qu et al., 2020; Huang et al., 2022; James et al., 2023), others attribute it to CB and RS (Grzegorczyk et al., 2025). Even for simulations of the same observational case, different modelling studies have produced conflicting estimates of how SIP mechanisms affect ice concentrations (Qu et al., 2022; Grzegorczyk et al., 2025). Differences in the representation of warm-rain processes across models may have potential impacts on the simulated SIP. Variations in how collision–coalescence efficiency, raindrop growth by accretion, and CCN activation are treated can all affect droplet sizes, while different entrainment parameterisations can influence the broadening of droplet distribution. These factors are particularly critical for SIP mechanisms such as RS and M2 that dependent on the presence of large droplets.

The structure of this paper is as follows. Section 2 introduces the DCMEX campaign and the case study. Section 3 describes the BMM configuration and the entrainment representation. Section 4 presents the results and the sensitivity analyses, followed by the discussion in Section 5 and the conclusions in Section 6.

2 DCMEX

2.1 Measurements

The DCMEX campaign was conducted in July and August 2022 over the Magdalena Mountains near Socorro, New Mexico, aimed to characterise the microphysics and dynamics of deep convective cloud formation, with one of its main challenges to better understand the secondary ice production mechanisms (Finney et al., 2024).

A key component of DCMEX was the Facility for Airborne Atmospheric Measurements (FAAM) British Aerospace Engineering-146 (BAE-146) aircraft, which was equipped with a comprehensive suite of aerosol and cloud microphysics instruments. During the DCMEX flights, the aircraft typically followed a kite-shaped pattern around the Magdalena Mountains. The right panel of Fig. 1 shows the flight track for Flight C300 on 22 July 2022, which is representative of the other flights that followed a similar plan view. All flights followed a similar pattern, starting with low-level aerosol runs to characterise the boundary-layer inflow, followed by cloud passes through developing convection to investigate microphysical properties within

https://doi.org/10.5194/egusphere-2026-302
Preprint. Discussion started: 11 February 2026

the mixed-phase region. In addition, dropsondes were released near the Magdalena Mountains to obtain vertical profiles of thermodynamic and wind fields (Finney et al., 2024). Below, we briefly summarise the instruments used in this study.

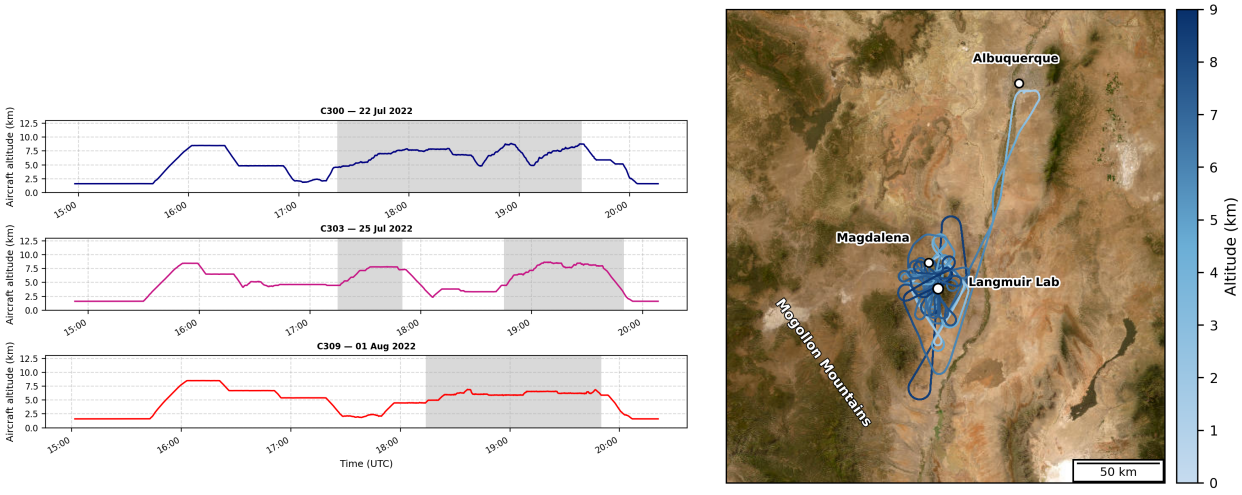

Figure 1. The left panel shows the time series of aircraft altitude for the three selected DCMEX cases, with shaded periods indicating cloud penetration. The right panel shows the corresponding flight track for the case on 22 July 2022 (C300).

The Aerosol Mass Spectrometer (AMS) and the Scanning Mobility Particle Sizer (SMPS) were used to measure the composition and size distribution of sub-micron aerosol. The AMS provided estimates of the effective κ of the aerosol, which were used to derive their Cloud Condensation Nuclei (CCN) properties for input into the Bin Microphysics Model (BMM). The SMPS was employed to characterise the aerosol size distribution near the cloud base, as shown in Wu et al. (2025).

The DMT cloud droplet probe (CDP-2) was used to measure droplet size distribution (DSD) (2–50 μm) and to derive cloud droplet number concentration (CDNC)(Lance et al., 2010b), whereas liquid water content (LWC) was obtained from a Nevzorov hot-wire probe following the Met Office processing method (Korolev et al., 1998; Abel et al., 2014).

The Cloud Particle Imager (CPI, version 2.5; SPEC Inc.) was used to obtain high-resolution images of cloud particles larger than 8 μm and to derive ice particle concentration. Although the CPI has a relatively small sample volume compared with the 2D-S, data from multiple flight segments were averaged to make the results more reliable and representative. The high-resolution imagery was also used to identify potential SIP mechanisms in this study (Korolev and Leisner, 2020; Korolev et al., 2022); further discussion is provided in Section. 4.3.

2.2 Case Study

The data used in this study were collected from 19 July to 7 August 2022 (flight C298–C314). In the early phase of the campaign, from 19 to 22 July (Flight C298–C300), the airmass originated from north-western (NW) flow from the Pacific over the continent towards the Magdalena Mountains, resulting in relatively lower cloud-base temperatures ($T_{\mathrm{cb}} \approx 1.5^{\circ}\mathrm{C}$) and lower humidity compared to later in the campaign. Around 24 July, a shift to south-eastern (SE) flow from the Gulf of Mexico

https://doi.org/10.5194/egusphere-2026-302
Preprint. Discussion started: 11 February 2026

introduced warmer and moister conditions, marking a transition observed in the subsequent flights (Flights C302–C314). After 28 July, the clouds generally maintained relatively high cloud-base temperatures ($T_{\mathrm{cb}} \approx 5.67°\mathrm{C}$) and relative humidity.

In this study, we focus on three representative cases, 22 July (C300), 25 July (C303), and 01 August (C309), which were selected based on the evolution of the airmass characteristics described above. The flight altitude for the three cases is shown in the left panel of Fig. 1. The 22 July case was chosen as it represents typical convective clouds that developed under the NW flow during the early phase of the campaign, while the 25 July case represents the early stage of SE inflow.

The 01 August case represents the later phase with SE flow. It was selected because the cloud was in a relatively early stage of development, before the convection had penetrated the detrainment layer. The in-situ sounding revealed a pronounced temperature inversion at around 7 km. However, the observed cloud top reached approximately 14.4 km (Finney et al., 2024), suggesting that the convection was strong enough to break through the inversion and later developed up to the tropopause. Such inversion-breaking convection is commonly observed over the mountainous southwest United States during the summer monsoon (Adams and Souza, 2009; Fonseca-Hernandez et al., 2021).

3 Bin microphysics parcel model

3.1 Model description

The model used in this study is the University of Manchester BMM, based on an updated version of the framework developed in previous studies (Topping et al., 2013; Fowler et al., 2020; James et al., 2023), with the source code available at https://github.com/UoM-maul1609/bin-microphysics-model . In the model, aerosols, cloud droplets and ice particles are represented on bin grids. The input aerosol size distribution for each external mixture j is expressed as the sum of M lognormal modes. The lognormal size distribution for each mode j is given by Equation 1.

$$\left[\frac{dN}{d\ln D}\right]_j = \sum_i^M \frac{N_{ap,i,j}}{\sqrt{2\pi}\ln\sigma_{g,i,j}} \exp\left(-\frac{\ln^2(D/d_{m,i,j})}{2\ln^2\sigma_{g,i,j}}\right) \tag{1}$$

where $\left[\frac{dN}{d\ln D}\right]_j$ is the aerosol number size distribution (cm^{-3}) for the external mixture j, D is the particle diameter (m), $N_{ap,i,j}$ is the total aerosol number concentration (cm^{-3}) of mode i within mixture j, $d_{m,i,j}$ is the geometric mean diameter (m), and $\sigma_{g,i,j}$ is the geometric standard deviation describing the width of the lognormal distribution. The summation over M modes allows representation of multi-modal aerosol populations (e.g. Aitken, accumulation and coarse modes) within each external mixture.

The model allows for several initial external mixtures of different composition, with aerosol composition represented by specifying a κ value for each mode j. In this study, a single externally mixed aerosol type is considered ($j = 1$), representing ammonium sulfate, consisting of two lognormal modes ($M = 2$) with a uniform hygroscopicity parameter (κ) across the size distribution.

https://doi.org/10.5194/egusphere-2026-302
Preprint. Discussion started: 11 February 2026

The aerosol size distribution is discretised into bins with the lowest bin edge set at 10 nm. The initial water mass associated with this bin is determined by solving for the zero of the Köhler equation. Each subsequent bin increases in water mass by a factor of $2^{1/2}$, resulting in a total of 140 bins. For each bin, the aerosol mass is calculated numerically using a root-finding algorithm to ensure consistency between the specified hygroscopicity parameter κ and the assigned water mass. The number concentration in each bin is then obtained by mapping Equation 1 onto the bin grid.

Condensation and evaporation processes are calculated using the variable-coefficient ordinary differential equation (VODE) solver from NETLIB library (Brown et al., 1989), which is well suited to handle the stiff nature of the associated differential equations. This approach ensures numerical stability and accuracy in representing droplet growth and evaporation across the bin grid.

For the ice phase, several additional prognostic variables are tracked in each bin. These include the crystal aspect ratio (Φ), the rime mass (ϱ), the number of crystal monomers per ice particle (N_{mon}), and the crystal density ($\rho_{crystal}$). It is further assumed that any rime mass freezes instantaneously upon accretion.

Collision–coalescence of cloud droplets, coagulation of aerosols, inertial impaction of aerosols, ice particle aggregation, and riming are represented by numerically solving the stochastic collection equation (SCE) using the exponential flux method of Bott (1998), with collision kernels from Jacobson (1999). During these collection processes, properties such as the total aerosol mass in colliding bins, as well as the ice-phase variables (Φ, ϱ, N_{mon}, and $\rho_{crystal}$), are consistently conserved during the collection processes.

3.2 Entrainment Representation

Two main approaches are considered to represent the entrainment process. In the BMM, homogeneous mixing is assumed, where environmental air continuously mixes with the parcel and is assumed to instantaneously dilute it at each time step. The resulting decrease in humidity reduces the growth rate of droplets of all sizes, and smaller droplets evaporate more rapidly as the relative humidity decreases, causing a shift of the droplet size distribution towards smaller diameters. This is implemented by including additional equations in the solver routine that are passed to VODE solver. The theory is described in Pruppacher and Klett (1997, chapter 12). The entrainment rate for a jet J is defined as

$$\mu_J = \frac{1}{F_m}\frac{dF_m}{dz} = \frac{C_J}{R_J} \tag{2}$$

where F_m is the total mass flux of the rising parcel (kg m^{-2} s^{-1}), $C_J \approx 0.2$ is the entrainment parameter, and R_J is the radius of the jet. The ascent of the parcel is calculated by considering the buoyancy and reaction of the surrounding air (see Equation 12.25 of Pruppacher and Klett, 1997).

The time evolution of the parcel's vertical velocity W (m s^{-1}) is described by

$$\frac{dW}{dt} = \frac{g}{1+\gamma}\left(\frac{T-T'}{T'} - w_L\right) - \frac{\mu}{1+\gamma}W^2 \tag{3}$$

https://doi.org/10.5194/egusphere-2026-302
Preprint. Discussion started: 11 February 2026

where g is the gravitational acceleration (9.81 m s^{-2}), $\gamma \approx 0.5$ is the moisture correction parameter accounting for the virtual effect of water vapour, T and T' are the temperatures of the parcel and the environment (K), respectively, w_L is the fractional mass of condensed liquid water relative to the total moist air, following Pruppacher and Klett (1997), and μ is the entrainment rate (m^{-1}), which accounts for momentum loss due to mixing with environmental air.

The radius of the jet changes during ascent according to

$$\frac{dR_J}{dt} = \frac{R_J}{2}\left(\mu_J W - \frac{1}{\rho}\frac{d\rho}{dt} - \frac{1}{W}\frac{dW}{dt}\right) \tag{4}$$

where R_J is the jet mass flux of the rising parcel (kg m^{-2} s^{-1}); t is time (s); μ_J is the entrainment rate (m^{-1}); W is the parcel vertical velocity (m s^{-1}); ρ is air density (kg m^{-3}); $d\rho/dt$ is the material rate of change of density (kg m^{-3} s^{-1}); and dW/dt is the vertical acceleration (m s^{-2}).

Finally, the water vapour mixing ratio is calculated by a statement of conservation of water substance

$$\frac{dw_v}{dt} = -\frac{dw_L}{dt} - \frac{dw_i}{dt} - \mu_J\left(w_v - w_v' + w_L + w_i\right) \tag{5}$$

where w_v is the water-vapour mixing ratio within the parcel (kg kg^{-1}); w_L is the liquid-water mixing ratio (kg kg^{-1}); w_i is the ice-water mixing ratio (kg kg^{-1}); t is time (s); μ_J is the entrainment rate (m^{-1}); and w_v' is the water-vapour mixing ratio of the entrained environmental air (kg kg^{-1}).

The BMM also allows entrainment to be represented as inhomogeneous mixing (Baker et al., 1980), in which environmental air is introduced into the parcel as discrete packets rather than being instantaneously mixed. The same mean entrainment rate as in the homogeneous case is applied, but mixing is implemented outside the VODE solver using discrete events over a longer 10,s timestep to represent intermittent entrainment. This formulation assumes that the mixing timescale is less than the evaporation timescale. Under this inhomogeneous mixing regime, small droplets in the entrained regions may completely evaporate while larger ones remain nearly unchanged. As a result, the total droplet number concentration becomes smaller than in the homogeneous case, producing greater supersaturation and enhanced condensational growth of the remaining droplets. Since the larger droplets are less affected by evaporation, collision–coalescence proceeds more efficiently, further accelerating droplet growth. A schematic of the two entrainment configurations is shown in Fig. 2.

3.3 Secondary ice parameterisations

The parameterisations of the four SIP mechanisms implemented in the BMM are based on the formulations of James et al. (2023). Rime splintering (RS) is parameterised following Reisner et al. (1998), which is based on the laboratory experiments of Hallett and Mossop (1974b). Splinter production is linked to the riming rate, which in the model is parameterised as the accretion of cloud droplets by graupel, considering the collection efficiency, relative fall velocity, and liquid water content. The process is active for $-7.5 \leq T \leq -2.5\,^{\circ}$C, with maximum efficiency near $-5\,^{\circ}$C.

https://doi.org/10.5194/egusphere-2026-302
Preprint. Discussion started: 11 February 2026

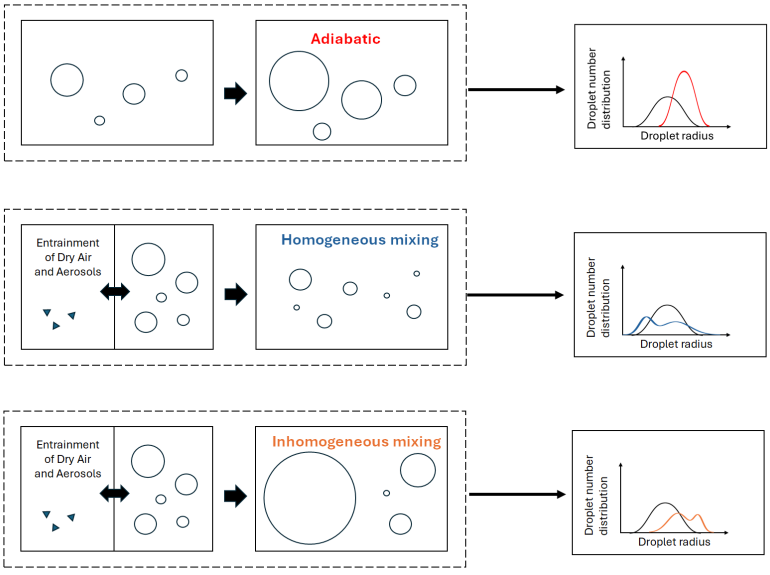

Figure 2. Schematic representation of the parcel model with a simplified entrainment–mixing framework, illustrating its influence on the droplet size distribution (DSD). The top panel shows the adiabatic case, without entrainment. The middle panel shows homogeneous mixing, where dry air and aerosols are uniformly mixed into the parcel. The bottom panel shows inhomogeneous mixing, in which environmental air is entrained as discrete packets. Adapted from (Lu et al., 2023).

Collisional breakup (CB) is parameterised following Phillips et al. (2017). The scheme relates fragment production to the collisional kinetic energy between ice particles, with efficiency modulated by ice particle type, density, riming, and aspect ratio. It accounts for collisions between graupel or hail, hail with hail, and snow or dendritic crystals with other ice particles.

Freezing fragmentation of drops is represented by two parameterisations from Phillips et al. (2018). Mode 1 (M1) describes the shattering of supercooled raindrops into multiple fragments upon freezing, with two size regimes distinguished: numerous small fragments and fewer large fragments, and is most efficient around $-15\,^{\circ}\mathrm{C}$. Mode 2 (M2) represents the fragmentation of supercooled drops upon collision with ice particles, controlled by the ratio of collisional kinetic energy to surface energy. Fragmentation occurs when drop diameters exceed 0.15 mm and the drop mass is smaller than that of the colliding ice particle, with the number of fragments depending on the collision energy.

3.4 Initial conditions

In our study, simulations are initialised at cloud base with an initial relative humidity of 0.95. All simulations are run for about 2.2 hours (8000s) with a timestep of 10 s, and the parcel radius is set to 1000 m. The initial aerosol size distribution is represented by a two-mode lognormal fit (see Fig. S1 and Table. S1). Table 1 summarises the initial aerosol and cloud-base

https://doi.org/10.5194/egusphere-2026-302
Preprint. Discussion started: 11 February 2026

conditions used to initialise the simulations, including the cloud-base pressure (P_{cb}), aerosol density (ρ), and hygroscopicity parameter (κ).

Table 1. Cloud-base thermodynamic and aerosol properties for the simulated cases, including the lifting condensation level (LCL), cloud-base temperature (T_{cb}), temperature perturbation (ΔT), cloud-base pressure (P_{cb}), updraught velocity (w_{cb}), aerosol density (ρ), and hygroscopicity parameter (κ).

Date	Flight	LCL (km)	T_{cb} (°C)	ΔT (K)	P_{cb} (hPa)	w_{cb} (m s^{-1})	ρ (kg m^{-3})	κ
Tue 19 Jul	C298	5.12	0.27	2.5	562.04	2.5	1566.84*	0.3811*
Wed 20 Jul	C299	4.99	1.47	0.2	571.23	1.0	1566.84	0.3811
Fri 22 Jul	C300	4.86	2.68	1.0	579.20	2.5	1484.95	0.2674
Sun 24 Jul	C302	4.10	5.44	1.0	635.06	2.5	1606.81	0.4149
Mon 25 Jul	C303	3.95	7.62	2.0	646.06	2.5	1617.27	0.4069
Tue 26 Jul	C304	3.92	7.06	2.0	648.35	1.0	1637.87	0.4461
Wed 27 Jul	C305	4.07	6.60	1.0	636.82	2.5	1650.06	0.4662
Fri 29 Jul	C306	4.06	5.98	2.5	636.90	2.5	1603.63	0.3939
Sat 30 Jul	C307	3.84	7.38	0.5	656.25	1.5	1571.12	0.4006
Sun 31 Jul	C308	4.39	2.77	2.0	613.79	2.5	1569.68	0.3824
Mon 1 Aug	C309	4.22	5.26	1.5	627.72	2.5	1547.22*	0.3482*
Tue 2 Aug	C310	4.29	4.97	1.0	621.02	1.0	1547.22	0.3482
Thu 4 Aug	C312	4.37	4.62	1.5	614.25	1.5	1591.61*	0.3921*
Sat 6 Aug	C313	4.31	5.16	1.0	619.58	1.0	1591.61	0.3921
Sun 7 Aug	C314	4.39	2.76	2.0	613.65	2.5	1541.35	0.3650

Values marked with an asterisk (*) were taken from a neighbouring case with similar atmospheric conditions because no data were available.

Seven simulations were performed for each case to represent the seven mixing scenarios considered in this study (see Table 2). These scenarios include two primary types of mixing, homogeneous (HOM) and inhomogeneous (INHOM), each examined with or without entrained aerosol (EA). For the inhomogeneous scenarios, we further distinguished whether the entrained aerosol particles were released (RA) following the mixing process. In addition, a fully adiabatic reference case (ADIA) was included.

In the BMM, the initial parcel temperature was set to the potential temperature with an added perturbation (ΔT). The value of ΔT and the initial updraught velocity at cloud base (w_{cb}) were both adjusted until the simulated LWC agreed with the upper boundary of the observed profiles, which aimed to model the cloud core where liquid water contents are typically high (Lehmann et al., 2009). For the adiabatic simulations, the ascent rate was constrained to match that in the non-adiabatic simulations, and the parcel was stopped at the same model cloud top. The entrainment parameter was set to 0 for the adiabatic simulations, while 0.2 was used for all non-adiabatic cases.

https://doi.org/10.5194/egusphere-2026-302
Preprint. Discussion started: 11 February 2026

Table 2. Summary of the mixing scenarios considered in this study. HOM: homogeneous mixing; INHOM: inhomogeneous mixing; EA: entrained aerosol; RA: released aerosol; ADIA: adiabatic case.

Scenario	Mixing type	Entrain aerosol	Release aerosol
HOM+EA	Homogeneous	Yes	–
HOM	Homogeneous	No	–
INHOM+EA+RA	Inhomogeneous	Yes	Yes
INHOM+RA	Inhomogeneous	No	Yes
INHOM+EA	Inhomogeneous	Yes	No
INHOM	Inhomogeneous	No	No
ADIA	Adiabatic	–	–

For each sensitivity experiment, the SIP mechanisms (RS, CB, M1, and M2) were investigated individually, as well as in simulations with all mechanisms switched off and with all mechanisms activated. We also performed sensitivity tests with the heterogeneous freezing parameterisations of Daily et al. (2025) and DeMott et al. (2010), given that SIP processes depend on the availability of primary ice crystals.

4 Results

We used the BMM to simulate the trajectories of individual air parcels for all 15 cases from the DCMEX campaign. Each parcel was initialised at the model cloud base and triggered by a thermal perturbation. Once the parcel reached buoyancy equilibrium, it remained at that level, while the internal microphysical processes and associated calculations continued throughout the simulation. Figures S2–S4 present the vertical profiles of CDNC, LWC, and D_{eff} for all simulated cases. Figure S5 shows the total ice crystal number concentration in the control simulation, where all SIP mechanisms were switched off and only primary ice from INP activation was considered, based on DCMEX INP measurements (Daily et al., 2025). Figures S6–S10 present the ice enhancement (i.e. the difference between the SIP ice crystal number concentration and control ice crystal number concentration), including simulations in which each SIP mechanism (RS, CB, M1, M2) is activated individually, as well as the configuration with all mechanisms activated together.

This section is organised into four parts. Section 4.1 presents the modelled evolution of liquid-phase properties (CDNC, LWC, and D_{eff}) for the three selected cases, and Section 4.2 shows the impact of entrainment on the droplet size distribution (DSD), including the vertical evolution of dispersion within the cloud. Section 4.3 compares observed and simulated clouds with all SIP mechanisms activated, and Section 4.4 analyses the contributions of individual SIP mechanisms.

https://doi.org/10.5194/egusphere-2026-302
Preprint. Discussion started: 11 February 2026

4.1 Bulk Liquid-Phase Cloud Properties

To quantify the contribution of SIP within the parcel, we first need to examine the liquid phase, including the vertical profiles of liquid water content (LWC), cloud droplet number concentration (CDNC), and D_{eff} from both observations and simulations under seven different mixing assumptions. The left panel of Figure 3 presents the evolution of LWC for the three selected cases, showing only small differences between the entrainment types because our parcel model entrains the same total mass of environmental air for both HOM and INHOM simulations. The simulations closely reproduce the maximum values of the observations, reaching peak values of approximately 1.0, 1.25, and 1.25 g m^{-3} near the parcel model maximum height. As expected, the observed values of LWC are much less than the adiabatic values due mainly to entrainment, while the ADIA simulations produce significantly higher LWC near the model cloud top, reaching approximately 300% of those in the HOM and INHOM simulations.

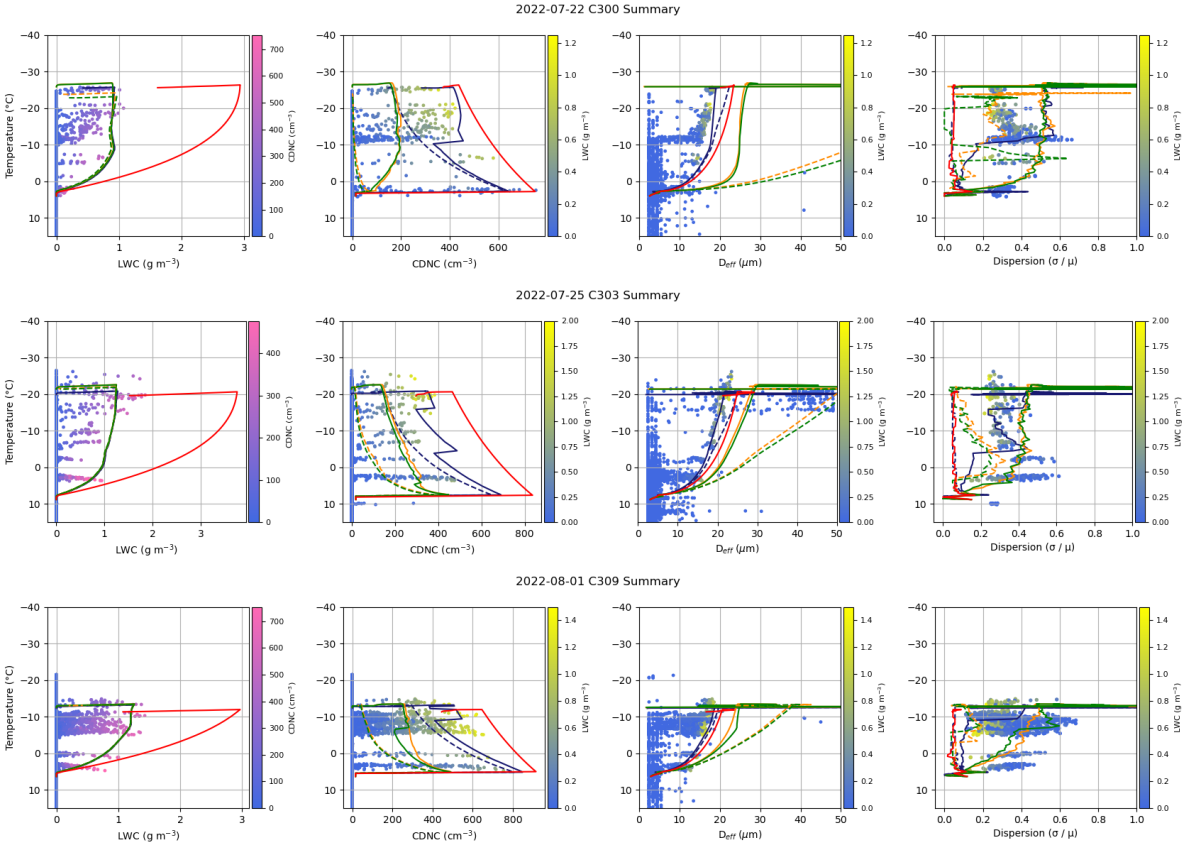

Figure 3. Vertical profiles of (from left to right): cloud droplet number concentration (CDNC), liquid water content (LWC), effective diameter (D_{eff}), and dispersion for three representative cases, C300 (22 July 2022), C303 (25 July 2022), and C309 (1 August 2022). Blue dots indicate observations; red lines denote ADIA; solid blue lines HOM+EA; dashed blue lines HOM; solid orange lines INHOM+EA+RA; dashed orange lines INHOM+RA; solid green lines INHOM+EA; and dashed green lines INHOM.

https://doi.org/10.5194/egusphere-2026-302
Preprint. Discussion started: 11 February 2026

It also should be noted that the CDP data collected during the DCMEX campaign represent instantaneous cloud measurements along the flight tracks, and the histories of the sampled cloud parcels cannot be determined. Therefore, the CDNC (middle-left panel), D_{eff} (middle-right panel), and dispersion (right panel) distributions of Figure 3 are interpreted in terms of LWC to identify cloud-core (yellow) and cloud-edge (blue) regions for each case. Following the findings of Lehmann et al. (2009), cloud-core regions are characterised by high liquid water content, as well as droplet concentrations and droplet size distributions that are broadly consistent with homogeneous mixing, whereas cloud-edge regions experience stronger evaporation, lower LWC, and are characterised by inhomogeneous mixing.

For the adiabatic simulations (ADIA), the maximum CDNC values were reached near the model cloud base, with approximately 750, 850, and 900 cm^{-3} for the 22 July, 25 July, and 1 August cases, respectively. CDNC decreased by approximately 20–40% as the parcel reached the model cloud top, mainly due to collision–coalescence, which remained active in the adiabatic simulations. In contrast, for the homogeneous mixing simulations, CDNC reached a peak of approximately 650, 700, and 850 cm^{-3} near the model cloud base for the three cases, respectively. At temperatures warmer than -10 °C, the HOM and HOM+EA simulations showed similar decreasing trends, with CDNC in HOM+EA remaining slightly higher. Around -10 °C, a second CDNC peak of approximately 450, 500, and 550 cm^{-3} appeared in HOM+EA, likely due to secondary droplet activation triggered by entrained aerosols. Near the model cloud top, CDNC in the HOM simulations was approximately 50% lower than in the HOM+EA simulations. Overall, the homogeneous mixing simulations with external aerosol entrainment (HOM+EA) show reasonable agreement with the upper envelope (yellow region) of the observed CDNC.

For the inhomogeneous mixing simulations, both INHOM+EA+RA and INHOM+EA reproduced the average observed CDNC reasonably well, showing similar vertical trends. When the entrainment of external aerosols was disabled (i.e., with EA turned off), CDNC in the INHOM+RA and INHOM simulations decreased significantly, with only a small number of droplets remaining near the model cloud top. The effect of released aerosol (RA) on CDNC under inhomogeneous mixing conditions was found to be limited, whereas the entrained aerosol (EA) significantly enhanced CDNC. This is likely because released aerosols form in regions of evaporation, where decreasing relative humidity and strong subsaturation prevents them from reaching the critical supersaturation required for activation. Among the inhomogeneous mixing simulations, INHOM+EA+RA showed reasonable agreement with the average observed CDNC.

Although the reduction in droplet number concentration under certain mixing conditions may slightly affect the efficiency of condensational growth, the overall impact on LWC remains limited. However, the ADIA simulations significantly overestimate LWC compared to observations, producing peak values approximately three times higher than those from simulations that include entrainment. As expected, D_{eff} increased with decreasing temperature as cloud developed. The HOM+EA simulations closely followed the upper envelope of the observations. In contrast, under inhomogeneous mixing without any entrained aerosol or aerosol recycling, D_{eff} reached unrealistically high values due to the dominance of a small number of large droplets. In these simulations, peak D_{eff} values reached approximately 90, 100, and 40μm in the three cases, respectively.

https://doi.org/10.5194/egusphere-2026-302
Preprint. Discussion started: 11 February 2026

4.2 Comparison of Observed and Modeled DSDs

The drop size distributions (DSDs) and corresponding dispersion for three representative cases (22 July, 25 July, and 1 August) were simulated and compared with in-situ aircraft observations. Figures S11–S13 show the vertical profiles of DSDs at nine selected temperature levels, from the cloud base to the cloud top, for each case. In the 22 July case, the observed D_{eff} increased from approximately 16 μm at –5.0 °C to 19 μm at –25.2 °C, consistent with condensational and collisional droplet growth during ascent. Meanwhile, the dispersion generally increased with height, indicating a progressive broadening of the droplet size distribution as the cloud developed. Similar trends were also found in the 25 July and 1 August cases.

The right panels of Figure 3 show the simulated and observed dispersions for the three cases. The dispersion is smaller within the approximate cloud-core regions (yellow dots), around 0.2–0.3 near the observed cloud top, whereas larger values are found near the cloud edges (blue dots). This pattern suggests that the droplet distributions are likely broadened by entrainment, mixing, or turbulence. It should also be noted that the observed DSDs may appear more dispersed than they actually are due to instrumental effects Lance et al. (2010a). This is consistent with Faber et al. (2018), who found that the mean diameters generally agree within a few percent, whereas the median diameters are overestimated by about 5–15%, resulting in an artificial broadening and skewing of the spectra. Overall, ADIA and HOM simulations both show narrow DSDs, whereas the HOM+EA simulation reproduces key observed features of the in-situ DSDs, including a broader spectral width, the persistence of small droplets at higher altitudes, and a bimodal structure, which highlights the role of entrainment in DSD broadening, consistent with Lasher-Trapp et al. (2005) and Morrison et al. (2022).

The results show that homogeneous mixing (HOM+EA) alone cannot explain the observed droplet dispersion, particularly during the early stages of cloud development. In contrast, inhomogeneous mixing (INHOM+EA+RA) can generate sufficiently broad droplet spectra but tends to overestimate the presence of large droplets, producing excessively wide distributions. This suggests that real cloud evolution may involve an initial inhomogeneous phase followed by more homogeneous mixing (Wu et al., 2025). For the 22 July case, additional simulations were performed, applying INHOM+EA+RA followed by HOM+EA to examine the influence of early inhomogeneous mixing on cloud development. As shown in Fig. 4, when the inhomogeneous phase lasts less than 30 s, the simulated results approach those of fully homogeneous mixing, while durations longer than 30 s result in behaviour consistent with inhomogeneous mixing. However, a major limitation of the parcel model in this study is its simplified treatment of ascending thermal trajectories. The model assumes isolated and internally uniform parcels, whereas in real thermals, parcel trajectories evolve dynamically, with varying turbulence, humidity, and mutual entrainment between neighbouring parcels. The transition from inhomogeneous to homogeneous mixing applied here should therefore be regarded as an idealised approximation.

4.3 Observed and Simulated Ice-Phase Properties

We performed simulations for three representative cases under three typical mixing scenarios (HOM+EA, INHOM+EA+RA, and ADIA), as shown in Figures 5–7. For each scenario, the simulations including all SIP mechanisms (RS, CB, M1, and M2) were compared with the corresponding control simulations without SIP, together with the observations, to quantify the

https://doi.org/10.5194/egusphere-2026-302
Preprint. Discussion started: 11 February 2026

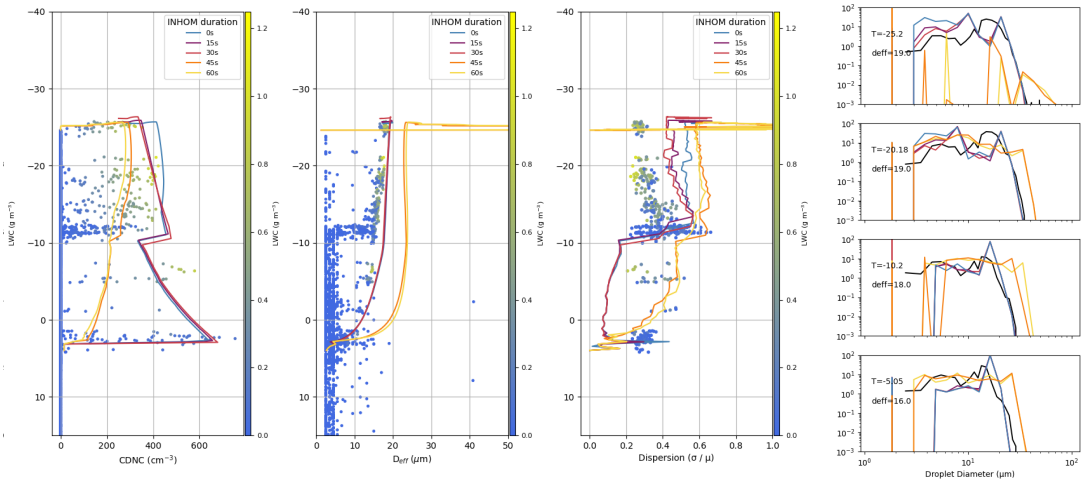

Figure 4. Vertical profiles of observed and simulated CDNC (left), D_{eff} (centre-left), and dispersion (centre-right), together with droplet size distributions (right) at four selected temperatures for the 22 July 2022 case. *INHOM duration* indicates the period of the INHOM+EA+RA phase in the combined INHOM+EA+RA–HOM+EA simulation.

impact of SIP on convective clouds during DCMEX. In this study, heterogeneous freezing was parameterised following Daily et al. (2025), and the simulated ICNC values were overall consistent with the INP curve reported by Daily et al. (2025). The parameterisation of DeMott et al. (2010) was also tested for comparison, and the results showed only minor differences between the two schemes.

For the 22 July case, the control ICNC peaked at approximately 20 L^{-1}, 10 L^{-1}, and 25 L^{-1} around 20 min in the ADIA, HOM+EA, and INHOM+EA+RA simulations, respectively. As shown in Fig. 5, HOM+EA produced almost no ice enhancement, whereas both ADIA and INHOM+EA+RA showed increases of about 20 L^{-1} (see the left panel of Fig. 9), with SIP in INHOM+EA+RA occurring roughly 20 min later than in ADIA. The simulated profiles need to be shifted downward to match the observations, likely because all particles remain within a single parcel without downdrafts or multiple thermals. In reality, ice particles are vertically transported, representing another limitation of the BMM framework. Similarly, for the 25 July and 1 August cases, the model underestimated ice concentrations below $-20^{\circ}\mathrm{C}$, mainly because the simplified parcel representation cannot capture the ongoing vertical transport of ice particles in real clouds.

For the south-easterly flow cases (25 July and 1 August), the control ICNCs were low, about 6 and 2 L^{-1}, respectively, and could not explain the observed ice concentrations. Only when SIP mechanisms were activated did the simulations reproduce the observed magnitudes, showing reasonable agreement with the measurements.

For the 25 July case, ADIA, HOM+EA, and INHOM+EA+RA produced ice enhancement at around 50, 90, and 95 min, reaching approximately 60, 40, and 20 L^{-1}, respectively. In the adiabatic simulation (ADIA), two peaks occurred at about 25 and 50 min, with maxima of roughly 20 and 60 L^{-1}. The homogeneous mixing simulation (HOM) produced a single peak

https://doi.org/10.5194/egusphere-2026-302
Preprint. Discussion started: 11 February 2026

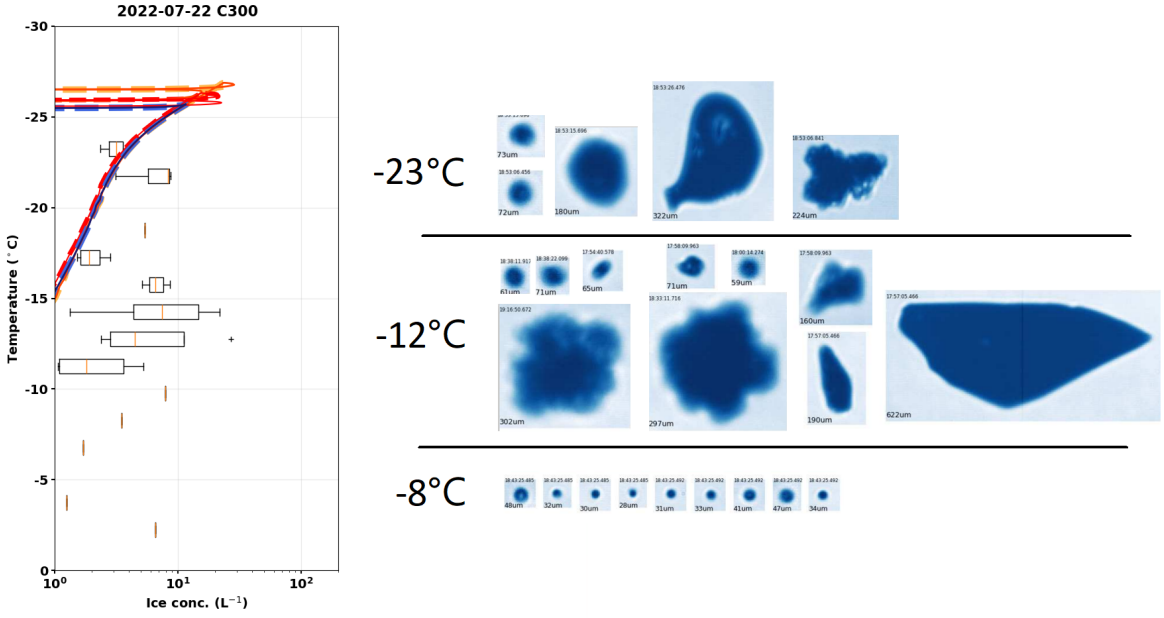

Figure 5. Vertical profiles of ice particle concentration and corresponding CPI imagery for the 22 July 2022 (C300) case. The left panel shows the observed (boxplots) and simulated ice concentrations from the parcel model under different entrainment scenarios, shown as a function of temperature. Blue, orange, and red lines represent the HOM+EA, INHOM+EA+RA, and ADIA simulations, respectively. Solid lines represent simulations with all SIP mechanisms activated, while dashed lines indicate simulations with SIP processes disabled. The right panel presents representative CPI images of ice particles sampled at approximately -8 °C, -12 °C, and -23 °C.

of about 35 L^{-1} near 105 min, whereas HOM+EA peaked earlier (90 min) at 45 L^{-1}. In contrast, both INHOM+RA and INHOM+EA+RA showed two peaks, at approximately 25 and 90 min, each reaching about 20 L^{-1}.

For the 1 August case, ADIA produced two peaks at around 40 and 70 min, both near 40 L^{-1}. INHOM+RA and INHOM+EA+RA also exhibited early enhancement at 40 min, reaching similar magnitudes. The homogeneous simulations showed later peaks, with HOM reaching about 20 L^{-1} at 110 min, and HOM+EA slightly earlier at 100 min with a maximum of 38 L^{-1}.

4.4 Analysis of Individual SIP Mechanisms

Sensitivity tests were conducted for all three cases to assess the individual contribution of the four SIP mechanisms (RS, CB, M1, and M2). For the 22 July case, RS produced a small ice enhancement of about 5 L^{-1} only in the INHOM+EA+RA simulation, occurring around 20 min. Most SIP activity appeared in the later stage of cloud development, when the parcel top temperature dropped below -25°C. RS conditions were not met when M2 conditions were active, and only M2 produced a noticeable ice increase.

https://doi.org/10.5194/egusphere-2026-302
Preprint. Discussion started: 11 February 2026

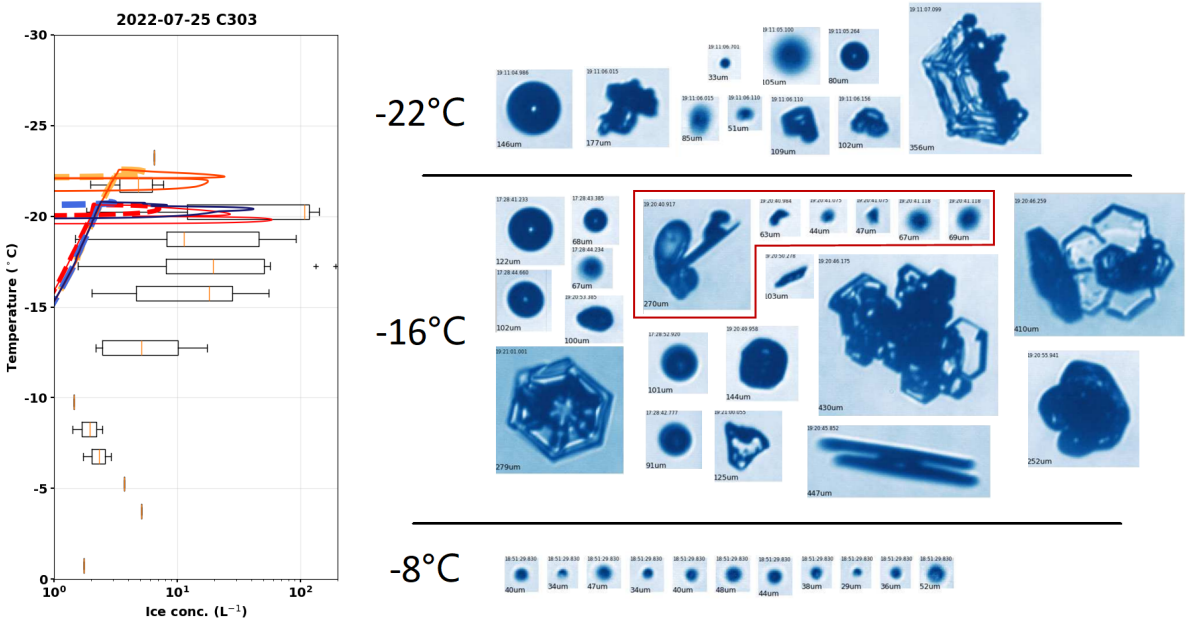

Figure 6. Vertical profiles of ice particle concentration and corresponding CPI imagery for the 25 July 2022 (C303) case. The left panel shows the observed (boxplots) and simulated ice concentrations from the parcel model under different entrainment scenarios, shown as a function of temperature. Coloured lines are as defined in Figure 5. The right panel presents representative CPI images of ice particles sampled at approximately $-8\,^{\circ}\mathrm{C}$, $-16\,^{\circ}\mathrm{C}$, and $-22\,^{\circ}\mathrm{C}$.

For the 25 July case, ice enhancement is likewise only observed when M2 is activated. In the inhomogeneous simulations without aerosol release (INHOM and INHOM+EA), large droplets appear early in the simulation, leading to ice enhancement around 20 min with peak values of approximately 20 L^{-1}. By contrast, the HOM+EA and the inhomogeneous simulations with aerosol release (INHOM+EA+RA and INHOM+RA) exhibit delayed ice enhancement, occurring at around 95 min with peak values of about 40 L^{-1} and 20 L^{-1}, respectively. When entrainment of aerosols is not considered (HOM), the onset of ice enhancement is further delayed, appearing roughly 20 min later and reaching peak values of around 30 L^{-1}. As shown in the right panel of Fig. 6, the CPI image displays a typical hexagonal crystal in the upper-right corner, likely formed after an ice–ice collision. The red box highlights features consistent with fragmentation between supercooled droplets and more massive ice particles (Mode 2).

For the 1 August case, RS produced no noticeable ice enhancement, as expected. In the INHOM+EA+RA, ADIA, and HOM+EA simulations, M2 generated ice enhancements of approximately 25, 40, and 30 L^{-1} at around 40, 80, and 110 min, respectively. When only the CB mechanism was activated, HOM+EA and INHOM+EA+RA showed additional ice enhancement of about 30 and 20 L^{-1} at around 100 and 70 min, respectively.

https://doi.org/10.5194/egusphere-2026-302
Preprint. Discussion started: 11 February 2026

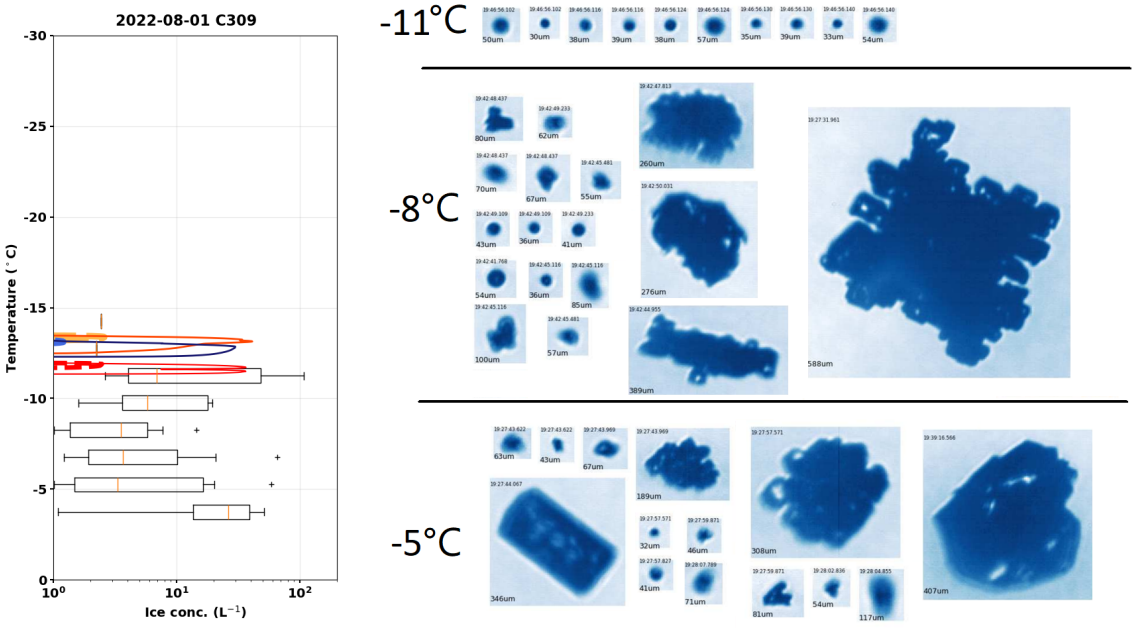

Figure 7. Vertical profiles of ice particle concentration and corresponding CPI imagery for the 1 August 2022 (C309) case. The left panel shows the observed (boxplots) and simulated ice concentrations from the parcel model under different entrainment scenarios, shown as a function of temperature. Coloured lines are as defined in Figure 5. The right panel presents representative CPI images of ice particles sampled at approximately -5 °C, -8 °C, and -11 °C.

5 Discussion

In our study, we investigated four SIP mechanisms (RS, CB, M1, and M2) in 15 deep convective cloud cases observed during the DCMEX campaign from 22 July to 7 August 2022 using a parcel model. Two entrainment representations (homogeneous and inhomogeneous mixing) were incorporated into the model, extending the adiabatic framework of James et al. (2023) to better represent dilution effects on cloud microphysics. Our results suggest that M2 is likely a key mechanism for explaining the high ice particle concentrations observed in deep convective clouds during the DCMEX campaign (see Figs. S6–S10). As for the other mechanisms, RS and M1 remained largely inactive across all 15 cases, while CB contributed to ice enhancement in some shallower cloud cases. M1 was likely not effective because collisions between large supercooled droplets and small ice crystals were rare, as shown by the CPI observations (Figs. 5–7). RS may be underestimated in a parcel model (see discussion later). However, observations during DCMEX indicate that RS contributed little to SIP in these clouds. This may partly result from the flight pattern adopted during the campaign, which could have limited sampling of regions where RS was active (P. J. Connolly, personal communication). The entrainment of aerosol was also found to accelerate the collision–coalescence process under homogeneous mixing conditions, leading to earlier ice enhancement, consistent with the hypothesis proposed by James et al. (2023).

https://doi.org/10.5194/egusphere-2026-302
Preprint. Discussion started: 11 February 2026

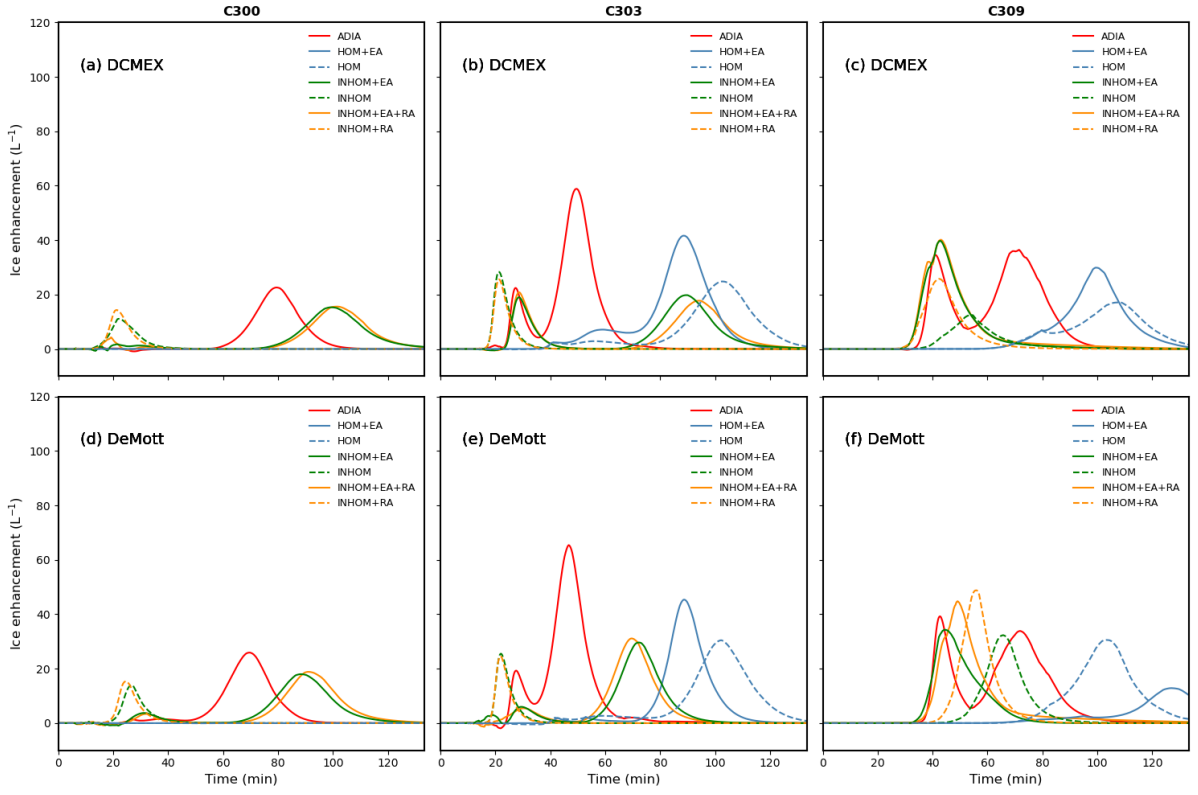

Figure 8. Time series of ice enhancement for three representative cases: C300 (left), C303 (middle), and C309 (right). The top row (a–c) shows simulations using the heterogeneous freezing parameterisation of Daily et al. (2025), while the bottom row (d–f) shows results using the parameterisation of DeMott et al. (2010). Colour coding follows Fig. 3.

To investigate the role of each SIP mechanism, it is first necessary to examine the development of the liquid phase during the early stages of cloud evolution. In our simulations, large droplets with diameters greater than 150 μm are critical for initiating M2, since droplets of this size with higher relative velocities are more likely to produce splashing during collisions. M2 becomes more active as the ratio of collision kinetic energy to surface energy increases in our BMM (Phillips et al., 2018; James et al., 2023). Previous studies have also shown that different representations of liquid-phase microphysics, especially the contrast between bulk and bin schemes (Lee and Baik, 2018; Johnson et al., 2024), can substantially affect the simulated efficiency of SIP. Grzegorczyk et al. (2025) and Qu et al. (2022) both analysed the same observational case of tropical deep convective clouds from the HAIC/HIWC campaign but reached contrasting conclusions regarding the contribution of droplet shattering (corresponding to our M1+M2) to ice enhancement, which they indicate differences in the availability of large droplets.

We found that representing aerosol entrainment was essential for simulating the observed breadth of the droplet size distribution during the DCMEX campaign. The observations revealed a bimodal spectrum with a distinct minimum near 10μm,

https://doi.org/10.5194/egusphere-2026-302
Preprint. Discussion started: 11 February 2026

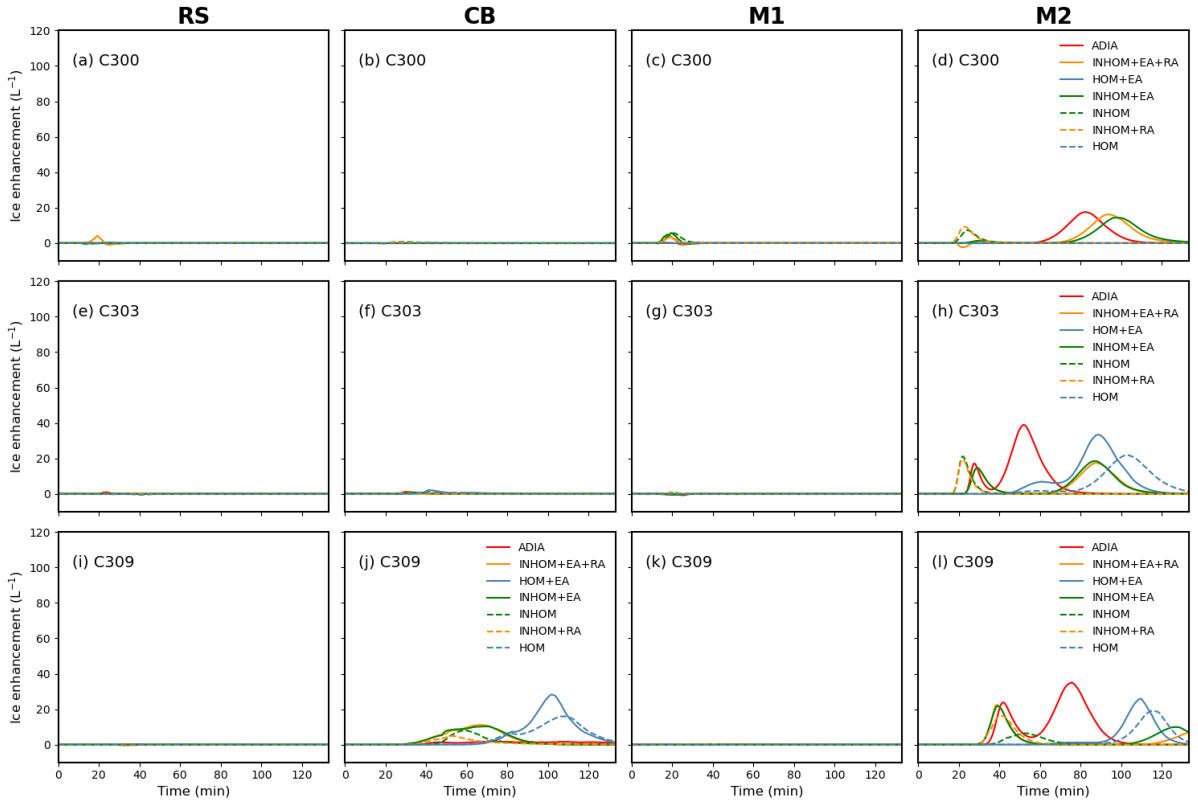

Figure 9. Time series of ice enhancement from individual SIP mechanisms for three representative cases: C300 (top row), C303 (middle row), and C309 (bottom row). Panels show the results for (a, e, i) rime splintering (RS), (b, f, j) collisional breakup (BR), (c, g, k) mode 1 freezing fragmentation (M1), and (d, h, l) mode 2 droplet–ice fragmentation (M2). Colour coding follows Fig. 3.

suggesting the presence of a secondary activation mechanism. This type of distribution has also been reported in previous studies (Morrison et al., 2022; Chandrakar et al., 2021; Cooper et al., 2013). James et al. (2023) also employed a parcel model to investigate the role of M2 in idealised shallow convective clouds. Their modelling setup is similar to our adiabatic configuration. Although adiabatic assumption can sometimes provide a reasonable approximation, observational and LES studies have shown that entrainment can begin almost immediately after cloud formation, with turbulent mixing potentially diluting the parcel even within a few hundred metres above cloud base (Grabowski and Wang, 2013). We found that the adiabatic simulations produced narrower droplet size distributions and tended to substantially overestimate CDNC, as well as LWC by up to approximately 300 %. As a result, the efficiency of secondary ice production was also overestimated, in some cases with relatively warm cloud-base temperatures and deeper cloud layers, such as C306 and C312, the enhancement of ice production was even two to three times greater than in the simulations that included entrainment. Simulations with inhomogeneous mixing tend to lead to an underestimation of CDNC and an overestimation of D_{eff}, as shown in Fig. 3. Although many previous studies suggest that inhomogeneous mixing tends to become more prevalent during later stages of the cloud life cycle, this is likely

https://doi.org/10.5194/egusphere-2026-302
Preprint. Discussion started: 11 February 2026

due to increased entrainment and evaporation near the cloud edges as the updraft weakens (e.g. Lehmann et al., 2009; Lim and Hoffmann, 2024; Xu et al., 2022). We did not find evidence supporting its dominance in our cases. This may be due to the aircraft tracking the developing clouds, thereby sampling them during the early stages of their lifecycle.

Despite the potential importance of entrainment for SIP, they have rarely been systematically evaluated in existing studies. Georgakaki et al. (2022) used the mesoscale model WRF with the Morrison double-moment microphysics scheme to investigate three SIP mechanisms, RS, CB and droplet shattering (corresponding to our M1 and M2) in two alpine clouds. They found CB to be the dominant contributor to SIP, while DS was inactive, likely due to the lack of large droplets. However, the Morrison double-moment scheme in WRF is closer to the homogeneous mixing limit in its evaporation–dilution representation. In our colder cloud-base case (C300), homogeneous mixing likewise produced no active SIP, whereas M2 became active under inhomogeneous mixing due to the production of large droplets. This suggests that the efficiency of DS in Georgakaki et al. (2022) may have been underestimated. A broad droplet size distribution can accelerate warm-rain formation through collision and coalescence, which can therefore affect SIP. Our results show that, across all SIP-active cases, HOM+EA leads to secondary ice enhancement occurring 15–20 minutes earlier and increasing in magnitude by approximately 30–40% compared with HOM. Sotiropoulou et al. (2020) used a high-resolution LES with double-moment bulk microphysics and explicitly resolved turbulent entrainment to investigate the effects of HM, BR and droplet fragmentation on summer Arctic stratocumulus. However, even at such high resolutions, the grid-scale microphysics in these models typically assumes instantaneous homogeneous mixing (e.g., Morrison and Grabowski, 2008). They found DS to be ineffective, yet this assumption cannot resolve the detailed evolution of the droplet size distribution under local dilution and may underestimate spectral broadening caused by size-dependent evaporation, potentially leading to an underestimation of DS.

In an earlier study of summertime cumuli over the same region in New Mexico, Blyth and Latham (1993) observed high ice crystal concentrations. They concluded that this enhancement could be explained by the Hallett–Mossop (HM) process, based on the observed coexistence of supercooled drizzle drops with radii greater than 24 μm and graupel near the RS temperature range. However, this is not supported by our results (see Fig. S11), as RS remains inactive throughout all 15 simulated cases. The clouds investigated in their study are similar to those observed during the DCMEX project in 2022. It also should be noted that the ice crystal concentrations reported by Blyth and Latham (1993) were likely significantly overestimated due to probe-induced shattering (Korolev et al., 2013; Jackson et al., 2014). In our simulations, the model results indicate that RS is not the dominant SIP mechanism in the early stage of cloud development (see Fig. S6). We also acknowledge that the parcel model, due to its simplified structure, may underestimate the contribution of the RS mechanism. During the ICE-T field campaign, Lasher-Trapp et al. (2016) reported cases in tropical maritime cumuli where graupel ascended near cloud tops and was later observed falling back into the rime-splintering zone, suggesting that RS could have been enhanced. Observations and simulations of tropical convective clouds during the ICE-D campaign by Cui et al. (2022) showed that the HM process was more active under multi-thermal conditions.

To assess the impact of primary ice nucleation on SIP, we tested two INP parameterizations, Daily (2025) and DeMott et al. (2010). The former is more appropriate for this study, as it was developed from measurements in the inflow clear air below cloud bases and in the environment around clouds during the DCMEX project, whereas the latter is a more general

https://doi.org/10.5194/egusphere-2026-302
Preprint. Discussion started: 11 February 2026

parameterization. However, our simulations showed negligible differences in SIP efficiency between the two, suggesting that once secondary ice multiplication is triggered, the choice of INP parameterization has limited influence on the final ice particle concentrations under these convective conditions.

6 Conclusions

In this study, we implemented entrainment parameterisations in the bin microphysics parcel model, including two different mixing representations (homogeneous and inhomogeneous) and external aerosol entrainment. These schemes were applied to simulations of summer continental deep convective clouds over New Mexico to assess the impacts of dry air and aerosol entrainment on cloud microphysical properties and secondary ice production. The representation of entrainment leads to systematic differences in secondary ice production by modifying liquid-phase microphysical properties (e.g. cloud droplet number concentration, liquid water content, and droplet size distribution), thereby affecting both the efficiency and onset of ice enhancement.

Our results show that the observed broad and bimodal droplet size distribution can only be reproduced when entrainment is included, particularly aerosol entrainment, within the parcel model framework for individual air trajectories. This is consistent with previous studies on the effects of dilution on the warm phase of clouds. In our adiabatic parcel simulations, cloud droplet number concentration and liquid water content are much higher than in simulations that include entrainment, with liquid water content exceeding entrainment cases by up to ∼300%. As a result, ice enhancement is up to 2–3 times larger in some cases. Under homogeneous mixing, aerosol entrainment tends to result in a broader droplet size distribution, with the SIP peak occurring 15–20 min earlier and reaching a higher peak value (by about 25%) than in simulations without aerosol entrainment. For shallow cloud cases, aerosol entrainment has little impact on SIP under inhomogeneous mixing. In deep cloud cases, inhomogeneous mixing results in an early SIP maximum (within ∼20 min) associated with an excess of large droplets; however, aerosol entrainment shifts the SIP peak to a timing comparable to that under homogeneous mixing. In our simulations of the DCMEX cases over New Mexico, most cases are best represented by homogeneous mixing combined with aerosol entrainment. We also find no evidence that inhomogeneous mixing dominates in the simulated clouds, which may be due to the aircraft primarily sampling clouds during their early stages of development.

When the four SIP mechanisms (RS, CB, M1, M2) are examined separately, our results suggest that M2 is the dominant contributor to ice enhancement in the DCMEX deep convective cloud cases. M1 remains largely inactive, likely due to limitations of the parcel model in which the absence of sedimentation leads to an accumulation of ice crystals and a progressive reduction in supercooled liquid water, thereby suppressing collisions between large droplets and small ice crystals required for efficient M1. CB contributes to ice enhancement in some shallower cloud cases but produces little ice enhancement in the deeper cloud cases. Our results suggest that RS alone cannot account for the high ice crystal concentrations observed during DCMEX. This contrasts with earlier interpretations for summertime cumuli over the same region, which attributed ice enhancement mainly to the Hallett–Mossop process (Blyth and Latham, 1993). In our simulations, RS is inefficient during the early stages of cloud development because the temperature range favourable for rime splintering does not coincide with the presence of sufficiently

https://doi.org/10.5194/egusphere-2026-302
Preprint. Discussion started: 11 February 2026

large droplets and ice particles. The contribution of RS may be underestimated in the parcel model framework, as multi-thermal circulations and interactions between different air parcels are not represented. Future extensions of the model that include sedimentation and interactions between different air parcels will therefore be required to better assess the potential role of RS in deep convective clouds.

Further progress in understanding M2 will require improved laboratory constraints on freezing-drop fragmentation and continued development of idealised parcel modelling frameworks that include sedimentation and interactions between different air parcels. Incorporating the effects of entrainment on secondary ice production will also be critical for achieving an accurate representation of ice-phase processes in numerical weather prediction and other large-scale models.

Code and data availability. The University of Manchester bin microphysics parcel model is available upon request. The model output data generated in this study will be deposited in Figshare, a FAIR-aligned (findable, accessible, interoperable and re-usable) data repository, and made publicly available upon acceptance of the manuscript.

https://doi.org/10.5194/egusphere-2026-302
Preprint. Discussion started: 11 February 2026

Author contributions. BZP and PJC conceived the original study. PJC developed the model code. BZP performed the simulations, analysed the data, and wrote the manuscript. HW provided key observational data. PJC, AMB and RLJ contributed to scientific discussions and provided comments on the manuscript.

Competing interests. The authors declare that they have no conflict of interest.

Acknowledgements. Airborne data were obtained using the FAAM Airborne Laboratory BAe-146 Atmospheric Research Aircraft, operated by Airtask Ltd, managed by the National Centre for Atmospheric Science, leased through the University of Leeds, and owned by UK Research and Innovation and the Natural Environment Research Council.

This project (author PJC) has received funding from the Horizon Europe programme under Grant Agreement No. 101137680.

The author used ChatGPT to assist with language editing and improving the clarity of the manuscript. All scientific analysis, interpretations, and conclusions were performed by the authors.

https://doi.org/10.5194/egusphere-2026-302
Preprint. Discussion started: 11 February 2026

References

Abel, S. J., Cotton, R. J., Barrett, P. A., and Vance, A. K.: A comparison of ice water content measurement techniques on the FAAM BAe-146 aircraft, Atmospheric Measurement Techniques, 7, 3007–3022, https://doi.org/10.5194/amt-7-3007-2014, 2014.

Adams, D. K. and Comrie, A. C.: The north American monsoon, Bulletin of the American Meteorological Society, 78, 2197–2214, 1997.

Adams, D. K. and Souza, E. P.: CAPE and convective events in the Southwest during the North American monsoon, Monthly Weather Review, 137, 83–98, 2009.

Baker, M. B., Corbin, R. G., and Latham, J.: The influence of entrainment on the evolution of cloud droplet spectra: I. A model of inhomogeneous mixing, Q. J. R. Meteorol. Soc., 106, 581–598, https://doi.org/https://doi.org/10.1002/qj.49710644914, 1980.

Billault-Roux, A.-C., Georgakaki, P., Gehring, J., Jaffeux, L., Schwarzenboeck, A., Coutris, P., Nenes, A., and Berne, A.: Distinct secondary ice production processes observed in radar Doppler spectra: insights from a case study, Atmospheric Chemistry and Physics, 23, 10 207–10 234, https://doi.org/10.5194/acp-23-10207-2023, 2023.

Blyth, A. M. and Latham, J.: Development of ice and precipitation in New Mexican summertime cumulus clouds, Quarterly Journal of the Royal Meteorological Society, 119, 91–120, https://doi.org/https://doi.org/10.1002/qj.49711950905, 1993.

Bott, A.: A flux method for the numerical solution of the stochastic collection equation, J. Atmos. Sci., 55, 2284–2293, 1998.

Brown, P. N., Byrne, G. D., and Hindmarsh, A. C.: VODE: A variable-coefficient ODE solver, SIAM journal on scientific and statistical computing, 10, 1038–1051, 1989.

Chandrakar, K. K., Grabowski, W. W., Morrison, H., and Bryan, G. H.: Impact of Entrainment Mixing and Turbulent Fluctuations on Droplet Size Distributions in a Cumulus Cloud: An Investigation Using Lagrangian Microphysics with a Subgrid-Scale Model, Journal of the Atmospheric Sciences, 78, 2983 – 3005, https://doi.org/10.1175/JAS-D-20-0281.1, 2021.

Cooper, W. A., Lasher-Trapp, S. G., and Blyth, A. M.: The Influence of Entrainment and Mixing on the Initial Formation of Rain in a Warm Cumulus Cloud, Journal of the Atmospheric Sciences, 70, 1727 – 1743, https://doi.org/10.1175/JAS-D-12-0128.1, 2013.

Crawford, I., Bower, K. N., Choularton, T. W., Dearden, C., Crosier, J., Westbrook, C., Capes, G., Coe, H., Connolly, P. J., Dorsey, J. R., Gallagher, M. W., Williams, P., Trembath, J., Cui, Z., and Blyth, A.: Ice formation and development in aged, wintertime cumulus over the UK: observations and modelling, Atmos. Chem. Phys., 12, 4963–4985, https://doi.org/10.5194/acp-12-4963-2012, 2012.

Cui, Z., Blyth, A., Huang, Y., Lloyd, G., Choularton, T., Bower, K., Field, P., Hawker, R., and Bennett, L.: Multi-thermals and high concentrations of secondary ice: a modelling study of convective clouds during the Ice in Clouds Experiment – Dust (ICE-D) campaign, Atmospheric Chemistry and Physics, 22, 1649–1667, https://doi.org/10.5194/acp-22-1649-2022, 2022.

Daily, M. I., Robinson, J., Finney, D. L., Raif, E. N., McQuaid, J. B., Sánchez-Marroquín, A., Hu, K., Lloyd, G., Flynn, M., Field, P. R., et al.: Ice-nucleating particle and cloud ice crystal concentrations associated with developing summertime deep convective clouds in south-western USA, Authorea Preprints, 2025.

DeMott, P. J., Prenni, A. J., Liu, X., Kreidenweis, S. M., Petters, M. D., Twohy, C. H., Richardson, M. S., Eidhammer, T., and Rogers, D. C.: Predicting global atmospheric ice nuclei distributions and their impacts on climate, Proc. Natl. Acad. Sci. U.S.A., 107, 11 217–11 222, https://doi.org/10.1073/pnas.0910818107, 2010.

Erfani, E. and Mitchell, D.: A partial mechanistic understanding of the North American monsoon, Journal of Geophysical Research: Atmospheres, 119, 13–096, 2014.

Faber, S., French, J. R., and Jackson, R.: Laboratory and in-flight evaluation of measurement uncertainties from a commercial Cloud Droplet Probe (CDP), Atmospheric Measurement Techniques, 11, 3645–3659, https://doi.org/10.5194/amt-11-3645-2018, 2018.

https://doi.org/10.5194/egusphere-2026-302
Preprint. Discussion started: 11 February 2026

Field, P. R. and Heymsfield, A. J.: Importance of snow to global precipitation, Geophys. Res. Lett., 42, 9512–9520, https://doi.org/https://doi.org/10.1002/2015GL065497, 2015.

Field, P. R., Lawson, R. P., Brown, P. R. A., Lloyd, G., Westbrook, C., Moisseev, D., Miltenberger, A., Nenes, A., Blyth, A., Choularton, T., Connolly, P., Buehl, J., Crosier, J., Cui, Z., Dearden, C., DeMott, P., Flossmann, A., Heymsfield, A., Huang, Y., Kalesse, H., Kanji, Z. A., Korolev, A., Kirchgaessner, A., Lasher-Trapp, S., Leisner, T., McFarquhar, G., Phillips, V., Stith, J., and Sullivan, S.: Secondary Ice Production: Current State of the Science and Recommendations for the Future, Meteorol. Monogr., 58, 7.1–7.20, https://doi.org/10.1175/AMSMONOGRAPHS-D-16-0014.1, 2017.

Finney, D. L., Blyth, A. M., Gallagher, M., Wu, H., Nott, G. J., Biggerstaff, M. I., Sonnenfeld, R. G., Daily, M., Walker, D., Dufton, D., Bower, K., Böing, S., Choularton, T., Crosier, J., Groves, J., Field, P. R., Coe, H., Murray, B. J., Lloyd, G., Marsden, N. A., Flynn, M., Hu, K., Thamban, N. M., Williams, P. I., Connolly, P. J., McQuaid, J. B., Robinson, J., Cui, Z., Burton, R. R., Carrie, G., Moore, R., Abel, S. J., Tiddeman, D., and Aulich, G.: Deep Convective Microphysics Experiment (DCMEX) coordinated aircraft and ground observations: microphysics, aerosol, and dynamics during cumulonimbus development, Earth System Science Data, 16, 2141–2163, https://doi.org/10.5194/essd-16-2141-2024, 2024.

Fonseca-Hernandez, M., Turrent, C., Mayor, Y. G., and Tereshchenko, I.: Using observational and reanalysis data to explore the southern Gulf of California boundary layer during the North American monsoon onset, Journal of Geophysical Research: Atmospheres, 126, e2020JD033 508, 2021.

Fowler, K., Connolly, P., and Topping, D.: Modelling the effect of condensed-phase diffusion on the homogeneous nucleation of ice in ultra-viscous particles, Atmos. Chem. Phys., 20, 683–698, https://doi.org/10.5194/acp-20-683-2020, 2020.

Grabowski, W. W. and Wang, L.-P.: Growth of Cloud Droplets in a Turbulent Environment, Annu. Rev. Fluid Mech, 45, 293–324, https://doi.org/10.1146/annurev-fluid-011212-140750, 2013.

Grzegorczyk, P., Yadav, S., Zanger, F., Theis, A., Mitra, S. K., Borrmann, S., and Szakáll, M.: Fragmentation of ice particles: laboratory experiments on graupel–graupel and graupel–snowflake collisions, Atmospheric Chemistry and Physics, 23, 13 505–13 521, https://doi.org/10.5194/acp-23-13505-2023, 2023.

Grzegorczyk, P., Wobrock, W., Canzi, A., Niquet, L., Tridon, F., and Planche, C.: Investigating secondary ice production in a deep convective cloud with a 3D bin microphysics model: Part I - Sensitivity study of microphysical processes representations, Atmospheric Research, 313, 107 774, https://doi.org/https://doi.org/10.1016/j.atmosres.2024.107774, 2025.

Hallett, J. and Mossop, S.: Production of secondary ice particles during the riming process, Nature, 249, 26–28, 1974a.

Hallett, J. and Mossop, S. C.: Production of secondary ice particles during the riming process, Nature, 249, 26–28, https://doi.org/10.1038/249026a0, 1974b.

Hallett, J., Sax, R. I., Lamb, D., and Murty, A. R.: Aircraft measurements of ice in Florida cumuli, Quarterly Journal of the Royal Meteorological Society, 104, 631–651, 1978.

Harris-Hobbs, R. L. and Cooper, W. A.: Field evidence supporting quantitative predictions of secondary ice production rates, Journal of Atmospheric Sciences, 44, 1071–1082, 1987.

Huang, Y., Chubb, T., Baumgardner, D., deHoog, M., Siems, S. T., and Manton, M. J.: Evidence for secondary ice production in Southern Ocean open cellular convection, Q. J. R. Meteorol. Soc., 143, 1685–1703, https://doi.org/https://doi.org/10.1002/qj.3041, 2017.

Huang, Y., Wu, W., McFarquhar, G. M., Xue, M., Morrison, H., Milbrandt, J., Korolev, A. V., Hu, Y., Qu, Z., Wolde, M., Nguyen, C., Schwarzenboeck, A., and Heckman, I.: Microphysical processes producing high ice water contents (HIWCs) in tropical convec-

https://doi.org/10.5194/egusphere-2026-302
Preprint. Discussion started: 11 February 2026

tive clouds during the HAIC-HIWC field campaign: dominant role of secondary ice production, Atmos. Chem. Phys., 22, 2365–2384, https://doi.org/10.5194/acp-22-2365-2022, 2022.

Jackson, R. C., McFarquhar, G. M., Stith, J., Beals, M., Shaw, R. A., Jensen, J., Fugal, J., and Korolev, A.: An assessment of the impact of antishattering tips and artifact removal techniques on cloud ice size distributions measured by the 2D cloud probe, Journal of Atmospheric and Oceanic Technology, 31, 2567–2590, 2014.

Jacobson, M. Z.: Fundamentals of atmospheric modeling, Cambridge university press, 1999.

James, R. L., Phillips, V. T. J., and Connolly, P. J.: Secondary ice production during the break-up of freezing water drops on impact with ice particles, Atmos. Chem. Phys., 21, 18 519–18 530, https://doi.org/10.5194/acp-21-18519-2021, 2021.

James, R. L., Crosier, J., and Connolly, P. J.: A bin microphysics parcel model investigation of secondary ice formation in an idealised shallow convective cloud, Atmospheric Chemistry and Physics, 23, 9099–9121, https://doi.org/10.5194/acp-23-9099-2023, 2023.

Johnson, M., Xue, M., and Jung, Y.: Comparison of a Spectral Bin and Two Multi-Moment Bulk Microphysics Schemes for Supercell Simulation: Investigation into Key Processes Responsible for Hydrometeor Distributions and Precipitation, Advances in Atmospheric Sciences, 41, 784–800, 2024.

Keinert, A., Spannagel, D., Leisner, T., and Kiselev, A.: Secondary ice production upon freezing of freely falling drizzle droplets, Journal of the Atmospheric Sciences, 77, 2959–2967, 2020.

Korolev, A. and Leisner, T.: Review of experimental studies of secondary ice production, Atmospheric Chemistry and Physics, 20, 11 767–11 797, https://doi.org/10.5194/acp-20-11767-2020, 2020.

Korolev, A., Strapp, J., Isaac, G., and Nevzorov, A.: The Nevzorov airborne hot-wire LWC–TWC probe: Principle of operation and performance characteristics, Journal of Atmospheric and Oceanic Technology, 15, 1495–1510, 1998.

Korolev, A., Emery, E., and Creelman, K.: Modification and tests of particle probe tips to mitigate effects of ice shattering, Journal of Atmospheric and Oceanic Technology, 30, 690–708, 2013.

Korolev, A., Heckman, I., Wolde, M., Ackerman, A. S., Fridlind, A. M., Ladino, L. A., Lawson, R. P., Milbrandt, J., and Williams, E.: A new look at the environmental conditions favorable to secondary ice production, Atmospheric Chemistry and Physics, 20, 1391–1429, https://doi.org/10.5194/acp-20-1391-2020, 2020.

Korolev, A., DeMott, P. J., Heckman, I., Wolde, M., Williams, E., Smalley, D. J., and Donovan, M. F.: Observation of secondary ice production in clouds at low temperatures, Atmospheric Chemistry and Physics, 22, 13 103–13 113, https://doi.org/10.5194/acp-22-13103-2022, 2022.

Lance, S., Brock, C., Rogers, D., and Gordon, J.: Water droplet calibration of the Cloud Droplet Probe (CDP) and in-flight performance in liquid, ice and mixed-phase clouds during ARCPAC, Atmospheric Measurement Techniques, 3, 1683–1706, 2010a.

Lance, S., Brock, C. A., Rogers, D., and Gordon, J. A.: Water droplet calibration of the Cloud Droplet Probe (CDP) and in-flight performance in liquid, ice and mixed-phase clouds during ARCPAC, Atmospheric Measurement Techniques, 3, 1683–1706, https://doi.org/10.5194/amt-3-1683-2010, 2010b.

Lasher-Trapp, S., Cooper, W., and Blyth, A.: Broadening of droplet size distributions from entrainment and mixing in a cumulus cloud, QJ Roy. Meteor. Soc., 131, 195–220, 2005.

Lasher-Trapp, S., Leon, D. C., DeMott, P. J., Villanueva-Birriel, C. M., Johnson, A. V., Moser, D. H., Tully, C. S., and Wu, W.: A multisensor investigation of rime splintering in tropical maritime cumuli, Journal of the Atmospheric Sciences, 73, 2547–2564, 2016.

Lasher-Trapp, S., Scott, E. L., Järvinen, E., Schnaiter, M., Waitz, F., DeMott, P. J., McCluskey, C. S., and Hill, T. C.: Observations and modeling of rime splintering in Southern Ocean cumuli, Journal of Geophysical Research: Atmospheres, 126, e2021JD035 479, 2021.

https://doi.org/10.5194/egusphere-2026-302
Preprint. Discussion started: 11 February 2026

Lauber, A., Kiselev, A., Pander, T., Handmann, P., and Leisner, T.: Secondary ice formation during freezing of levitated droplets, Journal of the Atmospheric Sciences, 75, 2815–2826, 2018.

Lawson, R. P., Woods, S., and Morrison, H.: The Microphysics of Ice and Precipitation Development in Tropical Cumulus Clouds, J. Atmos. Sci., 72, 2429 – 2445, https://doi.org/10.1175/JAS-D-14-0274.1, 2015.

Lee, H. and Baik, J.-J.: A Comparative Study of Bin and Bulk Cloud Microphysics Schemes in Simulating a Heavy Precipitation Case, Atmosphere, 9, https://doi.org/10.3390/atmos9120475, 2018.

Lehmann, K., Siebert, H., and Shaw, R.: Homogeneous and Inhomogeneous Mixing in Cumulus Clouds: Dependence on Local Turbulence Structure, Journal of The Atmospheric Sciences - J ATMOS SCI, 66, 3641–3659, https://doi.org/10.1175/2009JAS3012.1, 2009.

Leisner, T., Pander, T., Handmann, P., and Kiselev, A.: Secondary ice processes upon heterogeneous freezing of cloud droplets, in: 14th Conf. on Cloud Physics and Atmospheric Radiation, 2014.

Lim, J.-S. and Hoffmann, F.: Life cycle evolution of mixing in shallow cumulus clouds, Journal of Geophysical Research: Atmospheres, 129, e2023JD040 393, 2024.

Lloyd, G., Hu, K., Wu, H., Flynn, M., Bower, K., Marsden, N., Choularton, T., Daily, M., Murray, B., Coe, H., et al.: Overview of Secondary Ice Production In the Deep Convective Microphysics Experiment (DCMEX), 2024.

Lu, C., Liu, Y., Xu, X., Gao, S., and Sun, C.: Entrainment, mixing, and their microphysical influences, Fast Processes in Large-Scale Atmospheric Models: Progress, Challenges, and Opportunities, pp. 87–120, 2023.

Mignani, C., Creamean, J. M., Zimmermann, L., Alewell, C., and Conen, F.: New type of evidence for secondary ice formation at around $-15\,^{\circ}\mathrm{C}$ in mixed-phase clouds, Atmospheric Chemistry and Physics, 19, 877–886, https://doi.org/10.5194/acp-19-877-2019, 2019.

Morrison, H., Lawson, P., and Chandrakar, K. K.: Observed and Bin Model Simulated Evolution of Drop Size Distributions in High-Based Cumulus Congestus Over the United Arab Emirates, J. Geophys. Res.: Atmos., 127, e2021JD035 711, https://doi.org/https://doi.org/10.1029/2021JD035711, e2021JD035711 2021JD035711, 2022.

Mossop, S.: Some factors governing ice particle multiplication in cumulus clouds, Journal of Atmospheric Sciences, 35, 2033–2037, 1978.

Phillips, V. T., Patade, S., Gutierrez, J., and Bansemer, A.: Secondary Ice Production by Fragmentation of Freezing Drops: Formulation and Theory, J. Atmos. Sci., 76, 3031–3070, https://doi.org/10.1175/JAS-D-17-0190.1, 2018.

Phillips, V. T. J., Yano, J.-I., and Khain, A.: Ice Multiplication by Breakup in Ice–Ice Collisions. Part I: Theoretical Formulation, J. Atmos. Sci., 74, 1705 – 1719, https://doi.org/10.1175/JAS-D-16-0224.1, 2017.

Planche, C., Wobrock, W., and Flossmann, A. I.: The continuous melting process in a cloud-scale model using a bin microphysics scheme, Quarterly Journal of the Royal Meteorological Society, 140, 1986–1996, 2014.

Pruppacher, H. R. and Klett, J. D.: Microphysics of clouds and precipitation, "Norwell", 1997.

Qu, Y., Khain, A., Phillips, V., Ilotoviz, E., Shpund, J., Patade, S., and Chen, B.: The Role of Ice Splintering on Microphysics of Deep Convective Clouds Forming Under Different Aerosol Conditions: Simulations Using the Model With Spectral Bin Microphysics, J. Geophys. Res.: Atmos., 125, e2019JD031 312, https://doi.org/https://doi.org/10.1029/2019JD031312, e2019JD031312 2019JD031312, 2020.

Qu, Z., Korolev, A., Milbrandt, J. A., Heckman, I., Huang, Y., McFarquhar, G. M., Morrison, H., Wolde, M., and Nguyen, C.: The impacts of secondary ice production on microphysics and dynamics in tropical convection, Atmospheric Chemistry and Physics, 22, 12 287–12 310, https://doi.org/10.5194/acp-22-12287-2022, 2022.

Rangno, A. L. and Hobbs, P. V.: Ice particle concentrations and precipitation development in small polar maritime cumuliform clouds., Q. J. R. Meteorol. Soc., 117, 207–241, 1991.

https://doi.org/10.5194/egusphere-2026-302
Preprint. Discussion started: 11 February 2026

Reisner, J., Rasmussen, R. M., and Bruintjes, R. T.: Explicit forecasting of supercooled liquid water in winter storms using the MM5 mesoscale model, Q. J. R. Meteorol. Soc., 124, 1071–1107, https://doi.org/https://doi.org/10.1002/qj.49712454804, 1998.

Schwarzenboeck, A., Shcherbakov, V., Lefevre, R., Gayet, J.-F., Pointin, Y., and Duroure, C.: Indications for stellar-crystal fragmentation in Arctic clouds, Atmospheric Research, 92, 220–228, https://doi.org/https://doi.org/10.1016/j.atmosres.2008.10.002, 2009.

Seidel, J. S., Kiselev, A. A., Keinert, A., Stratmann, F., Leisner, T., and Hartmann, S.: Secondary ice production – no evidence of efficient rime-splintering mechanism, Atmospheric Chemistry and Physics, 24, 5247–5263, https://doi.org/10.5194/acp-24-5247-2024, 2024.

Sotiropoulou, G., Sullivan, S., Savre, J., Lloyd, G., Lachlan-Cope, T., Ekman, A. M. L., and Nenes, A.: The impact of secondary ice production on Arctic stratocumulus, Atmos. Chem. Phys., 20, 1301–1316, https://doi.org/10.5194/acp-20-1301-2020, 2020.

Takahashi, T. and Nagao, Y.: Possible high ice particle production during Graupel-Graupel collisions., Journal of the atmospheric sciences, 52, 1995.

Tan, I., Zhou, C., Lamy, A., and Stauffer, C. L.: Moderate climate sensitivity due to opposing mixed-phase cloud feedbacks, Npj Climate and Atmospheric Science, 8, 86, 2025.

Topping, D. O., Connolly, P. J., and McFiggans, G. B.: Cloud droplet number enhanced by co-condensation of organic vapours, Nature Geoscience, 6, 443–446, https://doi.org/10.1038/ngeo1809, 2013.

Vardiman, L.: The generation of secondary ice particles in clouds by crystal–crystal collision, Journal of Atmospheric Sciences, 35, 2168–2180, 1978.

Wu, H., Marsden, N., Connolly, P., Flynn, M., Williams, P., Finney, D., Hu, K., Nott, G. J., Thamban, N., Bower, K., Blyth, A., Gallagher, M., and Coe, H.: Observations of aerosol and cloud droplet formation in New Mexico summer deep-convection systems, In preparation, 1, 1–2, 2025.

Xu, X., Lu, C., Liu, Y., Luo, S., Zhou, X., Endo, S., Zhu, L., and Wang, Y.: Influences of an entrainment–mixing parameterization on numerical simulations of cumulus and stratocumulus clouds, Atmospheric Chemistry and Physics, 22, 5459–5475, https://doi.org/10.5194/acp-22-5459-2022, 2022.

Zhao, X. and Liu, X.: Primary and secondary ice production: interactions and their relative importance, Atmos. Chem. Phys., 22, 2585–2600, https://doi.org/10.5194/acp-22-2585-2022, 2022.